

Local versus global stability in dynamical systems with consecutive Hopf bifurcations

Philipp C. Böttcher^{1,2,*}, Benjamin Schäfer³, Stefan Kettemann⁴, Carsten Agert⁵, and Dirk Witthaut^{1,2,6}

¹*Institute of Energy and Climate Research, Systems Analysis and Technology Evaluation (IEK-STE),
Forschungszentrum Jülich, 52428 Jülich, Germany*

²*Institute of Energy and Climate Research, Energy Systems Engineering (IEK-10), Forschungszentrum Jülich, 52428 Jülich, Germany*

³*Institute for Automation and Applied Informatics (IAI), Karlsruhe Institute of Technology (KIT),
Hermann-von-Helmholtz-Platz 1, 76344 Eggenstein-Leopoldshafen, Germany*

⁴*School of Computer Science & Engineering, Constructor University, Campus Ring 1, 28759 Bremen, Germany*

⁵*DLR Institute of Networked Energy Systems, Carl-von-Ossietsky Straße 15, 26129 Oldenburg, Germany*

⁶*Institute for Theoretical Physics, University of Cologne, Zùlpicher Straße 77, 50937 Cologne, Germany*



(Received 7 March 2023; accepted 27 July 2023; published 29 August 2023)

Quantifying the stability of an equilibrium is central in the theory of dynamical systems as well as in engineering and control. A comprehensive picture must include the response to both small and large perturbations, leading to the concepts of local (linear) and global stability. Here, we show how systems displaying Hopf bifurcations show contrarian results for these two aspects of stability: Global stability is large close to the point where the system loses its stability altogether. We demonstrate this effect for an elementary model system, an anharmonic oscillator, and a realistic model of power system dynamics with delayed control. Detailed investigations of the bifurcation explain the seeming paradox in terms of the location of the attractors relative to the equilibrium.

DOI: [10.1103/PhysRevResearch.5.033139](https://doi.org/10.1103/PhysRevResearch.5.033139)

I. INTRODUCTION

Stability is an essential concept in the study of dynamical systems across disciplines [1]. Given a perturbation, does a system relax back to a desired equilibrium state or not? A loss of stability can have catastrophic consequences, for instance, the collapse of an ecosystem [2], the tipping of an element of the climate system [3], or a blackout of technical infrastructure such as the power grid [4]. Large perturbations are particularly hard to grasp, and one typically has to resort to extensive numerical simulations to assess the stability of an equilibrium. In this paper, we demonstrate a surprising aspect of stability in the presence of large perturbations: Certain systems are most stable when one expects the opposite, just before they become entirely unstable.

Traditionally, local stability has been central in the study of dynamical systems in the physical sciences. For a system in equilibrium affected by a small perturbation, the equations of motion can be linearized around its equilibrium point [1]. The resulting Jacobian matrix gives a comprehensive picture of the dynamics in the neighborhood of the equilibrium according to the Hartman-Grobman theorem [5]. If all eigenvalues of the Jacobian matrix have a negative real part, then small perturbations will relax exponentially fast back to the equilibrium point. Thus we denote this equilibrium as linearly stable. Note

that there are different definitions of local stability with the weakest one being Lyapunov stability. For an equilibrium that is Lyapunov stable, the dynamics stays close to the equilibrium but does not necessarily converge to it. In this paper, we will focus on the linear or exponential stability described above, which is a type of asymptotic stability, to quantify the local stability of the equilibrium point (i.e., the fixed point).

Large perturbations are much more challenging to address as linearization around an equilibrium is no longer justified. In some cases it is possible to prove global stability in systems as diverse as neural networks and power systems [6–9], but in many cases one has to resort to numerical investigations. An important domain-independent concept to quantify the global stability is the basin of attraction \mathcal{B} [10]: the set of initial points in state space from which the system converges to a given attractor. The geometry of such a basin can be extremely complex, especially in large dimensions [11]. Its volume, however, can be evaluated by numerical simulations: Drawing E randomly sampled initial conditions from a range of suitable points, the relative volume of the basin of attraction of one fixed point is estimated as $S_{\mathcal{B}} = M/E$, where M is the number of initial conditions converging to that fixed point. If the sampling is extensive enough, the volume provides a quantitative measure of global stability, which can be interpreted as the likelihood of returning to an attractor after a random perturbation [12,13]. We will focus exclusively on the basin of fixed points and will not consider more complex attractors.

Local stability and global stability do not necessarily align [14]. Obviously, local (i.e., linear) stability is a necessary condition for a nonzero basin size, but little can be said beyond this statement. In this paper, we demonstrate that local stability and global stability can even behave in completely opposite ways. We introduce a class of systems where the basin size

*p.boettcher@fz-juelich.de

assumes its maximum at a bifurcation point where linear stability is lost. This surprising behavior is demonstrated both for stylized models which allow for an analytic treatment and for advanced models inspired by engineering applications. All three systems share the same basic mechanism: The variation of an external control parameter induces a series of consecutive super- and subcritical Hopf bifurcations. We find that large basins with slow reconvergence to the fixed point may explain this contrarian behavior.

Overall, we have to understand that stability is a concept with multiple facets where linear stability and basin size may provide complementary information [13,15] and local stability implies global stability only under specific conditions [16]. Furthermore, the basin size is obviously not the only measure that characterizes the global stability of a fixed point. A large basin size implies that a fixed point is typically stable in the presence of large displacements in phase space. However, it does not allow for any conclusions about the speed of reconvergence or the stability with respect to ongoing deterministic or stochastic perturbations.

We note that extensions of network stability and synchronization often still rely on linear stability [17], while extensions of basin stability in terms of “survivability” are concerned with the transient behavior of the system with respect to a fixed point [18] but do not provide further insights into the basin of attraction of individual fixed points. In the following, we focus on basin volume estimates to quantify the global stability of a system, and we use the terms “local stability” and “linear stability” as synonyms.

This paper is organized as follows: We first study a stylized model in Sec. II to introduce the basic mechanism. We then proceed to a more advanced model in Sec. III, a kicked anharmonic oscillator, for which some analytic insights can be drawn by discretizing the dynamics. Finally, we analyze a dynamical system inspired by the load-frequency control in electric power engineering in Sec. IV. Taking into account delays in the control cycle, the system shows a similar series of Hopf bifurcations.

II. PROTOTYPICAL SYSTEM

We will show the basic mechanism of how local and global stability yield contradicting results using a stylized model which allows for a fully analytic treatment. We consider a particle moving in the two-dimensional plane \mathbb{R}^2 , generalizing the standard form of the Hopf bifurcation. Using polar coordinates with radius r and angle ψ , the equations of motion read

$$\begin{aligned} \dot{r} &= \mu r - (1 + \mu)r^3 + \alpha r^5, \\ \dot{\psi} &= \omega + br^2. \end{aligned} \tag{1}$$

Here, the dot denotes the differentiation with respect to time, and μ , $\omega > 0$, $\alpha > 0$, and $b > 0$ are parameters. In the following, we analyze the system’s dynamics when the parameter μ is varied while all other parameters are kept fixed. In all numerical examples, we set $\alpha = 0.1$, $\omega = 1$, and $b = 1$.

Attractors are found by setting $\dot{r} = 0$. The resulting attractors for the previously mentioned parameters are illustrated in Fig. 1. The system always has a fixed point at $r^* = 0$.

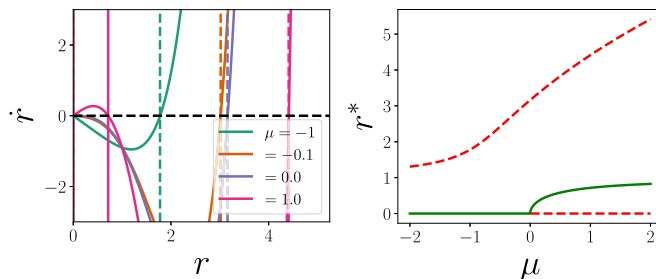


FIG. 1. Attractors in the prototypical system (1). Left: Visualization of the equations of motion. Fixed points or limit cycles are found where $\dot{r} = 0$ is the case, which is indicated by the solid and dashed vertical lines for stable and unstable limit cycles, respectively. Right: Bifurcation diagram. The radius of the stable attractors r^* is shown by the solid green lines, and the radius of the unstable fixed point and limit cycle is shown by the dashed red lines. A supercritical Hopf bifurcation occurs at $\mu = 0$.

Furthermore, limit cycles are found at the real positive roots of the polynomial equation

$$\mu - (1 + \mu)r^2 + \alpha r^4 = 0. \tag{2}$$

Varying the value of the parameter μ , we find the following scenario: For $\mu < 0$, the fixed point $r^* = 0$ is linearly stable, and one unstable limit cycle exists at a radius

$$r_2^2 = \frac{1 + \mu}{2\alpha} + \sqrt{\frac{(1 + \mu)^2}{4\alpha^2} - \frac{\mu}{\alpha}}.$$

A supercritical Hopf bifurcation takes place at $\mu = 0$. For $\mu > 0$, the fixed point is unstable, and a stable limit cycle exists at

$$r_1^2 = \frac{1 + \mu}{2\alpha} - \sqrt{\frac{(1 + \mu)^2}{4\alpha^2} - \frac{\mu}{\alpha}}.$$

Let us first consider the local stability of the fixed point $r^* = 0$. Using Cartesian coordinates, the linearized dynamics reads

$$\frac{d}{dt} \begin{pmatrix} x \\ y \end{pmatrix} = \underbrace{\begin{pmatrix} \mu & -\omega \\ \omega & \mu \end{pmatrix}}_{=: \mathbf{J}} \begin{pmatrix} x \\ y \end{pmatrix}, \tag{3}$$

and the eigenvalues of the Jacobian \mathbf{J} are found as $\lambda_{\pm} = \mu \pm i\omega$. The real part, which encodes the linear stability of the fixed point, is directly given by the parameter μ . The fixed point is stable for $\mu < 0$, and stability is lost at $\mu = 0$ in a Hopf bifurcation.

Now we turn back to global stability. We can directly read off the basin of attraction of the fixed point $r^* = 0$ for $\mu < 0$,

$$\mathcal{B}_{r^*} = \{\bar{x} \in \mathbb{R}^2 \mid \|\bar{x}\| < r_2\}, \tag{4}$$

and we can use r_2 to quantify the basin size. For $\mu \geq 0$, the fixed point $r^* = 0$ is unstable, and we set the basin size to zero for the sake of convenience.

The basin of attraction is shown together with the limit cycles in Fig. 2 for three values of μ . We find that the local stability and the global stability behave in opposite ways. As μ increases from negative values towards zero, the unstable limit cycle moves outwards such that the basin of attraction of

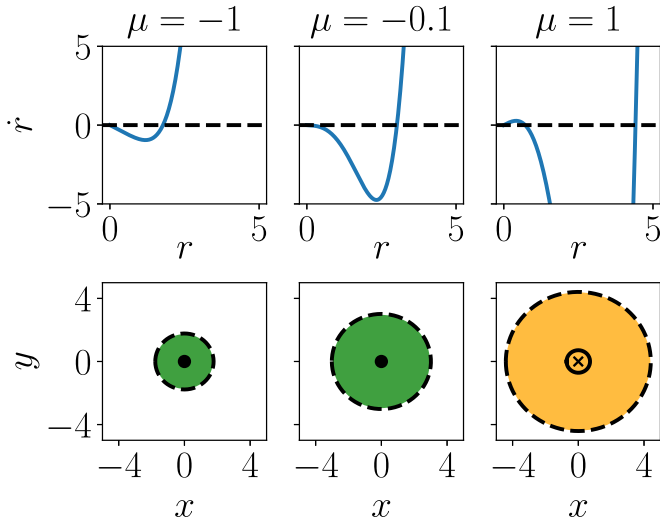


FIG. 2. The basin of the fixed point is limited by the surrounding limit cycle. Upper panels: Visualization of the equations of motion (1) for $\mu = -1, -0.1, 1$ (from left to right). Fixed points or limit cycles are found where $\dot{r} = 0$. Lower panels: Stable and unstable fixed points (dot and cross, respectively) and stable and unstable limit cycles (solid and dashed lines, respectively) in the plane. The green area shows the basin of attraction of the stable fixed point. A Hopf bifurcation occurs at $\mu = 0$, where the fixed point loses stability and a new stable limit cycle emerges. The basin of the fixed point is bounded by the limit cycle, whose radius increases monotonically with the parameter μ . For $\mu > 0$ there is no basin of attraction since the fixed point is not stable.

the fixed point grows. However, the local stability of the fixed point weakens until it is lost in a Hopf bifurcation at $\mu = 0$. Summarizing, the system reaches its maximal global stability (in terms of basin volume) at the same time that linear stability is lost at the bifurcation point.

III. DRIVEN NONLINEAR OSCILLATOR

The contrarian behavior of global and local stability can generally be found in systems where limit cycles and fixed points coexist. This scenario can occur repeatedly in a system with consecutive super- and subcritical Hopf bifurcations, as we will now demonstrate for a more general model system. In particular, we examine a damped and driven anharmonic oscillator.

We emphasize that the generalization to higher-dimensional dynamical systems is not trivial. In contrast to the prototypical example discussed above, the basin of attraction is no longer bounded by unstable limit cycles. However, the basic mechanism remains similar: The basin of attraction of the fixed point grows as the limit cycles move outwards.

We assume that the complex amplitude $z \in \mathbb{C}$ evolves according to the equations of motion

$$\dot{z} = (i\omega(|z|) - \eta)z + g(|z|, t), \tag{5}$$

with η being the damping constant and i being the imaginary unit. Here, we consider that the oscillator is anharmonic, such that the frequency ω decreases monotonically with the

amplitude $|z|$. The driving function is periodic in time, i.e., $g(|z|, t + T) = g(|z|, t)$ for a given period $T \in \mathbb{R}_{>0}$. Furthermore, the strength increases with the amplitude such that $g(0, t) = 0$.

The dynamical system (5) always has a trivial fixed point $z^* = 0$, which we interpret as the desired equilibrium state. The stability of this fixed point—both local and global—crucially depends on the existence of limit cycles. We will analyze this relation in detail for two special realizations of the external driving.

A. Kicked system

We now consider the case of a periodically kicked system, which allows for an approximate analytical solution. The nonlinear driving term reads

$$g(|z|, t) = a \sum_{n=-\infty}^{+\infty} \delta(t - nT)|z| \tag{6}$$

with an amplitude $a > 0$. The nonlinear kicking is interpreted as

$$z(nT + \epsilon) - z(nT - \epsilon) = a|z(nT + \epsilon)|, \quad \epsilon \rightarrow 0. \tag{7}$$

Furthermore, we assume that the amplitude of the anharmonic oscillator decreases with the amplitude as

$$\omega(|z|) = \frac{\mu}{T(1 + |z|^2)}. \tag{8}$$

We will discuss the resulting dynamics as a function of the control parameter μ .

If the damping constant η is sufficiently small, we can simplify the dynamics by assuming that the amplitude and thus the frequency ω remain approximately constant between two kicks. Then we obtain

$$z((n + 1)T - \epsilon) \approx \exp\{i(\omega - \eta)T\} z(nT + \epsilon). \tag{9}$$

Defining $z_n = z(nT + \epsilon)$, we thus obtain a discrete map

$$z_{n+1} = e^{i\nu(|z_n|)} \cdot \gamma \cdot z_n + c|z_n| \tag{10}$$

with $\nu(|z_n|) = \omega(|z_n|)T$, $\gamma = e^{-\eta T} \in [0, 1]$, and $c = \gamma a > 0$.

Limit cycles with period T are found by evaluating the condition $z_{n+1} = z_n$. Writing $z = |z|e^{i\alpha}$, the fixed-point equation reads

$$e^{i\alpha}|z| = \gamma|z|e^{i(\alpha + \nu(|z|))} + c|z|. \tag{11}$$

For the nontrivial limit cycles, we can solve this equation for the amplitude and phase and obtain

$$\cos(\nu(|z|)) = \frac{1 + \gamma^2 - c^2}{2\gamma}, \tag{12}$$

$$\cos(\alpha) = \frac{1 - \gamma^2 + c^2}{2c}. \tag{13}$$

Since real solutions only exist if the right-hand side of both equations is in the interval $[-1, +1]$, we assume this from now on. Note that the function $\nu(|z|)$ critically determines whether limit cycles exist or not. For the function given in Eq. (8), we find the following behavior: For $\mu = 0$, we typically find no solution to Eq. (12) and thus no limit cycle. As μ increases, additional solutions come into being as illustrated in Fig. 3.

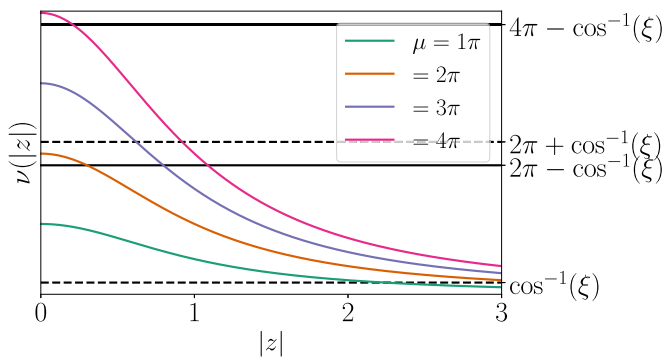


FIG. 3. Understanding the bifurcations in the kicked anharmonic oscillator as a function of the control parameter μ . Limit cycles are approximately determined by the solutions of Eq. (12). Unstable limit cycles are found for $v(|z|) = 2\pi n + \cos^{-1}(\xi)$, and stable limit cycles are found for $v(|z|) = 2\pi n - \cos^{-1}(\xi)$ with the abbreviation $\xi = (1 + \gamma^2 - c^2)/2\gamma$ and $n \in \mathbb{N}$. The figure shows the function $v(|z|)$ for different values of the control parameter μ . Stable (unstable) limit cycles exist where the function crosses the solid (dashed) horizontal lines.

The emerging limit cycles are alternately unstable and stable, and their amplitude $|z|$ increases monotonically with μ .

As a consequence, the phase space of the kicked system shows a characteristic structure for large values of μ : The trivial fixed point $z^* = 0$ is surrounded by multiple stable and unstable limit cycles. These limit cycles grow as μ increases, and new limit cycles emerge repeatedly via Hopf bifurcations. The fixed point becomes unstable when a new stable limit cycle emerges, and it becomes stable again when a new unstable limit cycle emerges.

The phase space structure determines the system’s global stability. The basin of attraction is shaped by coexisting competing attractors, which are the emerging limit cycles in this case. Since the size of the emerging limit cycles grows monotonically with μ , we expect that local stability and global stability behave in opposite ways and that the basin size assumes its maximum right before local stability is lost.

We test these qualitative statements by scanning the parameter μ in the range $[0, 20\pi]$ and simulating the discrete dynamics given by Eq. (10) numerically. To check which states run into different attractors, we chose the random complex initial condition $z_0 = z_{0,r} + z_{0,i}i$ by uniformly sampling the real part $z_{0,r}$ and the imaginary part $z_{0,i}$ from the interval $[-4, 4]$. The map is iterated for $t_n = 1000$ steps to check whether the discrete dynamics runs into an attractor. Since we are interested in how the trivial fixed point at $z^* = 0$ is affected by the other attractors, we quantify its global stability by counting the number of initial conditions that run into this fixed point; that is, S_B is the fraction of initial conditions that return to z^* .

Setting the parameters to $c = 0.5$, $\gamma = 0.9$, and $T = 1$, we find that the simulations confirm the expected behavior (see Fig. 4). As μ increases, the trivial fixed point repeatedly switches from stable to unstable as new limit cycles emerge. During the stable intervals, the basin size S_B of the fixed point increases monotonically with μ and assumes its maximum at the bifurcation point. Notably, the limit cycles undergo further

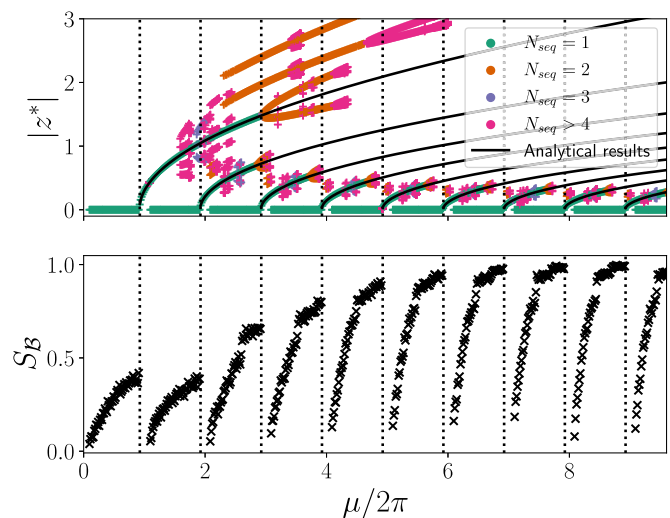


FIG. 4. Attractors and basin stability S_B of the discrete map [which approximates the kicked anharmonic oscillator (5)] as a function of the control parameter μ . Upper panel: Absolute value of the stable limit cycles with period N_{seq} . The trivial fixed point $z^* = 0$ undergoes a series of consecutive super- and subcritical Hopf bifurcations, where it changes from stable to unstable and vice versa. The positions of supercritical Hopf bifurcations are shown by the vertical black dotted lines, and the stable limit cycles, calculated by solving Eq. (12), are indicated by the solid black lines. Lower panel: The basin stability S_B of the trivial fixed point increases monotonically with μ until it jumps to zero when stability is lost in a supercritical Hopf bifurcation, which is indicated by the vertical black dotted lines. The relative basin size S_B was computed by sampling $E = 1000$ initial conditions at random from the subset $[-4, 4] \times [-4i, 4i]$ of the complex plane.

bifurcations which are not treated here as we focus on the stability of the fixed point.

B. Continuously driven system

To show that the analytical and numerical results also hold for a time-continuous system, we return to the original continuous dynamical system given in Eq. (5) and assume a continuous driving. We replace the delta function or more specifically the *kick* by using a Gauss function $\Lambda(t) = (2\pi)^{-\frac{1}{2}} \cdot \exp(-\frac{t^2}{2})$, which results in

$$g(|z|, t) = a \sum_{n=0}^{\infty} N_d \cdot \Lambda(N_d \cdot [t - nT]) \cdot |z|, \quad (14)$$

where $N_d \in \mathcal{N}$ is a positive constant. Using this substitute, we study the dynamics numerically as a function of the control parameter μ . We sample uniformly in $[-4, 4]$ to get both the real and imaginary parts of the initial conditions z_0 . Choosing the same parameters, i.e., $c = 0.5$, $\gamma = 0.9$, and $T = 1$, as in the discrete map, we solve the ordinary differential equation (ODE) in the time interval $t \in [0, 200]$. Only a short range (i.e., $t_c = 20$) at the end of the resulting time series is used to evaluate whether or not the trivial fixed point is reached. The size of the basin S_B is again given by the fraction of initial states that end in the trivial fixed point. The simulation results (see Fig. 5) confirm the qualitative picture

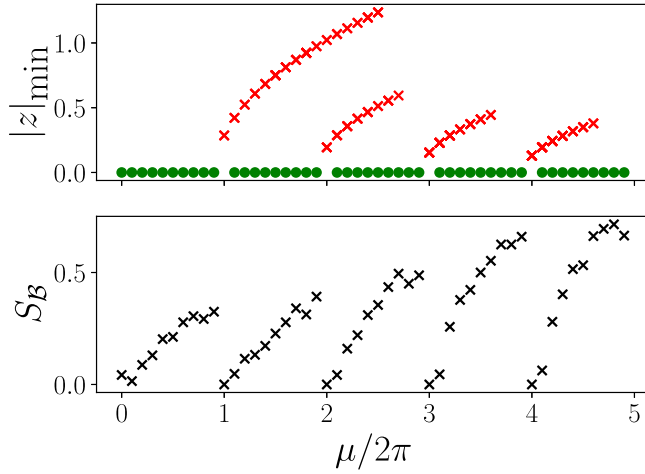


FIG. 5. Fixed points and limit cycles of the driven anharmonic oscillator (5) as a function of the control parameter μ . Top panel: For each stable fixed point or limit cycle with a period of $T = 1$, we plot the minimum of the magnitude $|z|_{\min}$. Green dots indicate where the trivial fixed point is stable, and red crosses show where stable limit cycles were detected. Bottom panel: Basin stability S_B for the trivial fixed point. The relative basin size S_B was computed by sampling $E = 400$ initial conditions at random from the subset $[-4, 4] \times [-4i, 4i]$ of the complex plane for every value of μ . The periodic driving is given by Eq. (14).

obtained for the discrete map. In particular, we again find that the local stability and global stability of the trivial fixed point have opposite behaviors. The upper panel of Fig. 5 shows the trivial fixed point surrounded by limit cycles that increase in diameter with increasing μ . Again the size of the basin of attraction increases with the diameter of the limit cycle and is largest slightly before the fixed point loses stability and a new limit cycle with small diameter appears. Note that as in the case of the discrete map there are more bifurcations present in the system that are hard to detect numerically. The limit cycles presented in Fig. 5 are only the stable ones that have a period of $T = 1$ and follow the same path in phase space.

IV. OSCILLATORS WITH DELAYED CONTROL

Hopf bifurcations often occur in delayed dynamical systems. Such a delay can arise in a feedback or control loop, where measurements and information processing require some time. We will now demonstrate that the previously introduced scenario of consecutive Hopf bifurcations may occur in a control system of immense practical importance: the load-frequency control of electric power systems [19–21].

A. Power system dynamics and control

We consider an aggregated model of an electric power grid [22,23], decomposing the grid into certain regions or control areas. The areas are strongly coupled internally, such that local differences in the grid frequency are negligible. Hence every area $i = 1, \dots, N$ is characterized by its voltage phase angle $\theta_i(t)$ and the frequency deviation $\omega_i(t) = \dot{\theta}_i(t)$ from the reference frequency ω_0 . Ideally, all areas should run at the same nominal reference frequency $\omega_0 = 2\pi \times 50$ Hz or

$\omega_0 = 2\pi \times 60$ Hz, but imbalances of power generation and load induce deviations. The load-frequency control measures these frequency deviations and adapts the generation to restore the balance and limit deviations from the reference state.

The dynamics of the aggregated model is described by the aggregated swing equation

$$\dot{\theta}_i(t) = \omega_i(t), \quad (15)$$

$$A_i \dot{\omega}_i(t) + k_{l,i} \omega_i(t) = P_{0,i}(t) + P_{c,i}(t) - \sum_j P_{ij}(t), \quad (16)$$

using a frame of reference rotating at the frequency ω_0 . Here, A_i quantifies the amount of inertia, and $k_{l,i}$ is a damping constant due to generator damper windings or frequency-dependent loads. Effectively, each area is modeled as an aggregated synchronous machine [23]. The right-hand side includes the balance of scheduled generation and load $P_{0,i}(t)$, the contribution of the load-frequency control system $P_{c,i}(t)$, and the flow to other areas given by

$$P_{ij}(t) = C_{ij} \sin(\theta_i(t) - \theta_j(t)). \quad (17)$$

The control system continuously monitors the grid and adapts the power $P_{c,i}(t)$ to restore the desired grid operation. Here we focus on primary control, also referred to as frequency containment reserve (FCR), which is activated within seconds [22]. Primary control can be described as a proportional controller, adjusting the power proportional to frequency deviations. Both measurement and communication as well as the activation of a reserve power plant require some time and are thus delayed by a few seconds [21]. We thus model primary control, following earlier work [15,24], as

$$P_{c,i}(t) = -k_{P,i} \omega_i(t - \tau) \quad (18)$$

with the time delay $\tau > 0$. In the following, systems with homogeneous gains $k_{P,i} = k_P$ and damping constants $k_{l,i} = k_l$ for all $i = 1, \dots, N$ are considered. Further control layers exist, which are activated on longer time scales and react to more intricate measurements of the system's state [22,25]. These will be neglected in this paper for the sake of clarity.

In summary, the dynamics is given by the delay differential equation (DDE)

$$\dot{\theta}_i(t) = \omega_i(t), \quad (19)$$

$$A \dot{\omega}_i(t) + k_l \omega_i(t) = P_{0,i} - k_P \omega_i(t - \tau) - \sum_j C_{ij} \sin(\theta_i(t) - \theta_j(t)), \quad (20)$$

where the control is delayed by the parameter $\tau > 0$ and works against a detected frequency deviation ω_i proportionally to the gain k_P .

B. Fixed points and oscillations

Ideally, the power grid should be at a fixed point where the power balances $P_{0,i}$ are fixed and all areas are perfectly synchronized,

$$\omega_i(t) = \omega^*, \quad (21)$$

$$\theta_i(t) = \theta_i^* + \omega^* t. \quad (22)$$

Recall that the variables θ_i and ω_i are defined in a rotating frame with reference frequency ω_0 . The fixed-point values are determined by the algebraic equations

$$P_{0,i} - (k_l + k_p)\omega^* = \sum_j C_{ij} \sin(\theta_i^* - \theta_j^*). \quad (23)$$

Summing over all areas $i = 1, \dots, N$, we further obtain

$$\omega^* = \frac{\sum_i P_{0,i}}{\sum_i (k_l + k_p)}.$$

Disturbances of the power balance can cause transient deviations from this fixed point. Interarea oscillations are a notable example of this behavior [26–28]; these are large-scale oscillations of the phases $\theta_i(t)$ and the power flows in Eq. (17) of the entire grid, potentially over thousands of kilometers. The eigenmodes are determined by the structure of the grid, with typical frequencies in the range of 0.1 Hz. Interarea oscillations are typically damped out in minutes.

In exceptional contingency situations, oscillations may also grow leading to a loss of synchrony in the grid and eventually a blackout. For instance, such an instability may arise after the loss of several transmission elements in a cascade of failures; see Ref. [28] for an example.

C. Linear stability analysis

In this section, we discuss the linear stability of the desired fixed point. To this end, we linearize the equations of motion (20) as $\theta_i(t) = \theta_i^* + \omega^*t + \alpha_i(t)$. To simplify the analysis, we assume that the grid is balanced in total such that $\sum_i P_{0,i} = 0$ and $\omega^* = 0$.

We then obtain the linearized equations

$$\dot{\alpha}_i = \omega_i, \quad (24)$$

$$A_i \dot{\omega}_i = -k_l \omega_i - k_p \omega_{i,\tau} - \sum_j L_{ij} \alpha_j. \quad (25)$$

Here, we have used the shorthand $\omega_{i,\tau} = \omega_i(t - \tau)$ and dropped all time dependencies for the sake of brevity. The coupling between the areas is described by the network Laplacian $\mathbf{L} \in \mathbb{R}^{N \times N}$ with elements

$$L_{ij} = \begin{cases} -C_{ij} \cos(\theta_i^* - \theta_j^*) & \text{if } i \neq j \\ \sum_{m \neq i} C_{im} \cos(\theta_i^* - \theta_m^*) & \text{if } i = j. \end{cases} \quad (26)$$

For further analysis we define a state vector

$$\vec{x} = (\alpha_1, \dots, \alpha_N, \omega_1, \dots, \omega_N)^\top$$

and rewrite the linearized equations in a matrix form

$$\mathbf{A} \dot{\vec{x}}(t) = \mathbf{N} \vec{x}(t) + \mathbf{D} \vec{x}(t - \tau). \quad (27)$$

with the block matrices

$$\mathbf{A} = \begin{pmatrix} \mathbb{I} & \mathbf{0} \\ \mathbf{0} & \hat{\mathbf{A}} \end{pmatrix}, \quad \mathbf{N} = \begin{pmatrix} \mathbf{0} & \mathbb{I} \\ -\mathbf{L} & -\mathbf{K}_l \end{pmatrix}, \quad \mathbf{D} = \begin{pmatrix} \mathbf{0} & \mathbf{0} \\ \mathbf{0} & -\mathbf{K}_p \end{pmatrix},$$

where $\hat{\mathbf{A}} = \text{diag}(A_1, \dots, A_N)$, $\mathbf{K}_p = k_p \mathbb{I}$, $\mathbf{K}_l = k_l \mathbb{I}$, and \mathbb{I} is the N -dimensional identity matrix. As Eq. (27) is a linear DDE with constant coefficients, it has eigenmodes of the form $\vec{x} = \vec{x}(t_0)^{\frac{1}{2}} (e^{\lambda t} + e^{\bar{\lambda} t})$ [29]. The characteristic roots λ and their

complex conjugate $\bar{\lambda}$ can be determined by using the exponential ansatz $\vec{x} = \vec{v} e^{\lambda t}$. The eigenvalues can thus be determined from the characteristic equation

$$\det(\lambda \mathbf{A} - (\mathbf{N} + \mathbf{D} e^{-\lambda \tau})) = 0. \quad (28)$$

As in the linear stability analysis of systems governed by ordinary differential equations, the stability is encoded in the signs of the eigenvalues λ_i , i.e., all solutions of Eq. (28). The fixed point is linearly stable if the real part of all eigenvalues is negative and unstable if the real part of at least one eigenvalue is positive [30]. The characteristic equation (28) is a transcendental equation with infinitely many solutions and is thus in general more challenging to solve compared with the case of ordinary differential equations. A reliable method to approximate the eigenvalue spectrum [i.e., the characteristic roots of Eq. (28)] is to use the Chebyshev collocation method [31,32]. It describes the state of the linearized delay differential equation $\vec{x}(\theta)$ in the time interval $[t - \tau, t]$ by discretizing at the so-called Chebyshev points $t_k = \cos(\frac{k}{N_C} \pi) \in [-1, 1]$ with $k = 0, \dots, N_C$ and N_C giving the number of Chebyshev points and thus the resolution. The DDE is now approximated as $\vec{y}(t) = [\vec{x}_0(t), \dots, \vec{x}_{N_C}(t)]^\top$, where $\vec{x}_k(t) = \vec{x}(t - \frac{\tau}{2}(t_k + 1))$. One now has a $K(N_C + 1)$ -dimensional state vector $\vec{y}(t)$ instead of the K -dimensional original state $\vec{x}(t)$ transforming the linear delay differential equation to $\dot{\vec{y}}(t) = \mathbf{M}_C \vec{y}(t)$ with \mathbf{M}_C given by

$$\mathbf{M}_C = \begin{pmatrix} -\frac{2C_M}{\tau} \otimes \mathbf{I}_K \\ \mathbf{A}^{-1} \mathbf{D}, \mathbf{0} \dots \mathbf{0}, \mathbf{A}^{-1} \mathbf{N} \end{pmatrix},$$

where C_M is the Chebyshev differentiation matrix with the last row being deleted, I_K is the K -dimensional identity matrix, and \otimes is the Kronecker product. Note that the last row in \mathbf{M}_C is the original delay differential equation, while the others represent a spectral approximate of the time derivative at the Chebyshev nodes.

In addition to approximating the eigenvalue spectrum using Chebyshev discretization, one can evaluate the points in parameter space, where an eigenvalue might pass the imaginary axis and a bifurcation occurs. To this end, we have used the software DDE-BIFTOOL [33] to identify bifurcation points and continue these points to obtain curves on which a bifurcation takes place. Furthermore, we employ DDE-BIFTOOL to determine the type of bifurcation by calculating normal form coefficients [34].

D. Global stability

The global stability of the power system model given in Eq. (20) is quantified in terms of the basin of attraction of the desired fixed point. However, measuring the size of the basin becomes challenging for delayed differential equations. It is not sufficient to choose a point in phase space to specify the initial state of the system. Instead, the function $\vec{x}_0(t')$ must be specified for $t' \in [t_0 - \tau, t_0]$. While it might be useful to tailor the specific initial function to the application at hand or sampling from a reasonable set of initial functions [35], the choice of initial functions is ultimately arbitrary, which makes it hard to make a general statement on the global stability of an attractor. To get around this problem, an efficient method to

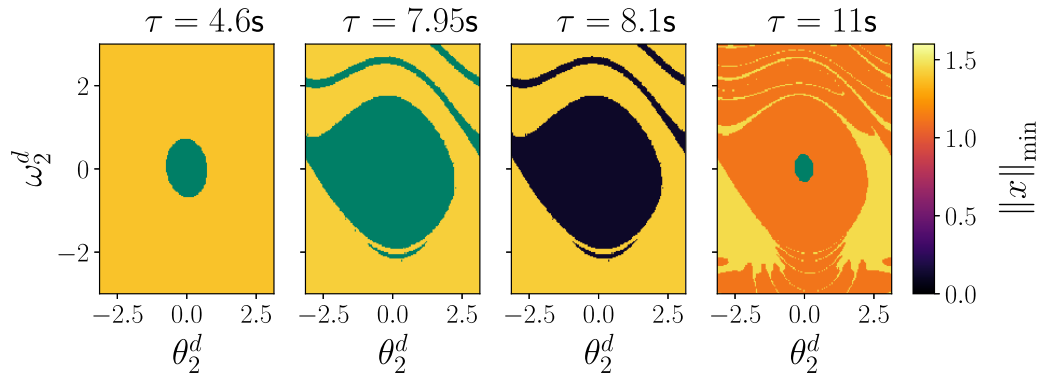


FIG. 6. Basin of the fixed point and surrounding limit cycles of the delayed differential equation describing power grid dynamics (20) for different values of the delay τ . Simulations were performed by disturbing the stationary frequency deviation and power phase angles of area 2 by ω_2^d and θ_2^d , respectively. From left to right, the values for τ were chosen as 4.6, 7.95, 8.1, and 11 s. The basin of the fixed point corresponding to operation at the reference frequency (i.e., $\omega_i = 0 \forall i$) is shown in green. The color scale describes the minimal 2-norm of the distance of the limit-cycle dynamics to the fixed point $\|x\|_{\min}$ showing the coexistence of different limit cycles.

assess global stability in delayed systems has been proposed in Refs. [36,37].

In principle, one chooses a suitable initial function segment and solves the delay differential equation. We will choose a constant past given by setting the state vector $x_0(t')$ to a constant value for $t' \in [t_0 - \tau, t_0]$. Keep in mind that a larger delay with the same initial constant effectively represents a larger disturbance. Thus it is useful to evaluate the L^2 -norm, which can be seen as the energy of a specific disturbance, of the initial function segment instead of the randomly chosen value that gives the constant past. To quantify how stable a fixed point is, the initial function with the smallest norm that does not result in the dynamics relaxing to the considered fixed points is of interest. This value gives the primary attractor radius, which is still a bad approximate for the size of the basin of attraction since it only considers constant-function segments. Subsequently, all simulations that did not return to the considered fixed points are used to get a better estimate for the size of the basin. By cutting them up into all possible segments of length τ , measuring the L^2 -norm of the segments, and keeping the minimum, the secondary attractor radius can be calculated. Choosing the minimum of the primary and secondary attractor radii results in the attractor radius R_a , which gives a measure for the smallest possible disturbance that results in the dynamics not relaxing to the considered fixed point.

While measuring the basin has its limitations [38] and this is even more true for systems that include delayed dynamics [35], knowledge of the attractor radius R_a can be used to examine how the approximate size of the basin changes for different parameters or, more specifically, which smallest disturbance leads to the attractor not being recovered.

E. Results

We now compute the local and global stability in a power grid model consisting of two areas with homogeneous parameters.

This model system captures essential physical processes, in particular the interplay of interarea oscillations and control systems, but still allows for a comprehensive visual

analysis. Choosing $k_p = 0.0625$, $k_l = 0.025$, $A = 1$ s, $C_{1,2} = 0.5$, and $P_{0,\{1,2\}} = \pm 0.0625$, we study the resulting dynamics and stability as a function of the delay time τ . We initialize the simulation by setting the initial function to the constant state $\bar{x}_0 = [\theta_1^0, \theta_2^0, \omega_1^0, \omega_2^0] = [\theta_1^*, \theta_2^* + \theta_2^d, 0, \omega_2^d]$ with ω_2^d and θ_2^d being the difference with respect to the stationary values of the frequency deviation and the power phase angle of the second area, respectively.

Figure 6 provides a first visual overview of the global stability for four different values of τ . In particular, Fig. 6 shows different attractors the system ends up in for different constant values, which define the function segments that serve as the initial state of the DDE given in Eq. (20).

The fixed point is linearly stable for $\tau = 4.6$ s but has a rather small basin of attraction. At the same time, we find an unstable limit cycle of small radius. Increasing the delay to $\tau = 7.95$ s, both the limit cycle and the basin grow. A further small increase in the delay to $\tau = 8.1$ s makes the desired fixed point unstable. For many initial function segments, the system now relaxes to a stable limit cycle with small amplitude indicating that a supercritical Hopf bifurcation took place. Finally, the fixed point regains its stability for $\tau = 11$ s, again with a comparatively small basin of attraction. Outside of this basin, the system relaxes to two different limit cycles for the chosen set of values defining the constant-initial-function segments. This highlights a similar structure of different attractors around the trivial fixed point as observed for the kicked anharmonic oscillator in Sec. III.

To gain further insight into the interaction of limit cycles and fixed points, we perform a bifurcation analysis using the software DDE-BIFTOOL [33] to complement the linear stability analysis of the fixed points described in Sec. IV C. The results shown in Fig. 7 reveal a series of consecutive super- and subcritical Hopf bifurcations, similar to the examples presented in Sec. III. Without delay, i.e., at $\tau = 0$ s, the fixed point is linearly stable. As τ increases, stability is lost in a supercritical Hopf bifurcation, and a stable limit cycle emerges. After a further increase in τ , stability is regained in a subcritical Hopf bifurcation where an unstable limit cycle emerges. This scenario repeats itself when the delay τ is increased further, leading to a characteristic structure of stable

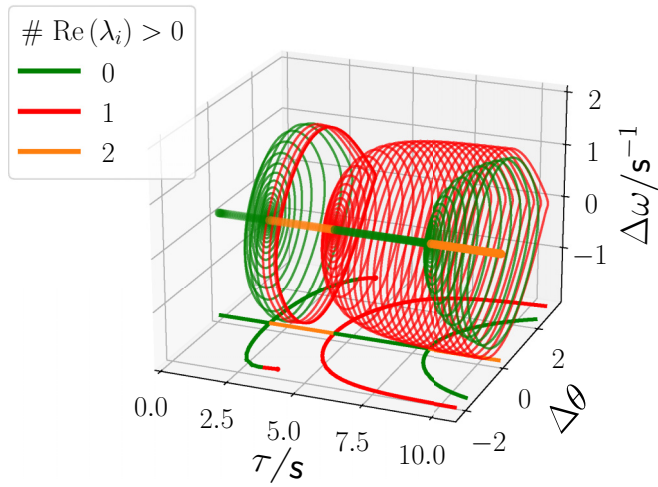


FIG. 7. Bifurcation diagram of the delayed dynamical system (20). Attractors for different values of the delay τ in the $\Delta\omega$ - $\Delta\theta$ plane with the difference in frequency deviations $\Delta\omega = \omega_2 - \omega_1$ and the difference in phase angles $\Delta\theta = \theta_2 - \theta_1$. The colors indicate the linear stability, given by the number of eigenvalues λ_i with a real part greater than zero, of the respective attractor. Here, green is encoding linear stability, while red and orange show that there are one and two unstable eigenvalues, respectively, such that the dynamics is linearly unstable. A projection of the cut through the attractors at $\Delta\omega = 0$ is shown below. We observe a set of consecutive super- and subcritical Hopf bifurcations and the coexistence of different limit cycles.

and unstable limit cycles in phase space. We recall that an unstable limit cycle does not bound the basin of attraction in dimensions higher than two. Nevertheless, we find a very similar behavior to that in the prototypical system and the anharmonic oscillator: The existence and location of stable and unstable limit cycles predict the basin of the fixed point.

We can now provide a comprehensive analysis of the local and global stability of the desired fixed point as a function of the delay τ . Figure 8 compares the location of limit cycles, the size of the basin of attraction, and the linear stability of the fixed point. As the delay τ increases, the fixed point repeatedly switches from stable to unstable and back. Mathematically, this corresponds to a set of super- and subcritical Hopf bifurcations as explained above. Physically, the instability can be explained as a resonance effect [24]. The delayed control amplifies the interarea eigenmode instead of damping it. Hence regions of instability are found where the delay τ matches an integer multiple of the period of the eigenmodes.

The limit cycles generally increase in size with the delay τ . This leads to opposite behaviors of the linear and global stability. Within the regions of stability, the basin typically grows monotonically with τ . Hence basin stability is large at the bifurcation, when the fixed point becomes unstable again. Remarkably, we find the highest value of the basin size for $\tau \approx 20$ s, at the edge of the fourth stability region.

Since the value of k_p is a choice that is given by the control design, it is important to understand how it affects the stability of the desired fixed point. The stability chart in Fig. 9 shows both the results of the linear stability analysis and the results obtained by finding the attractor radius R_a . The

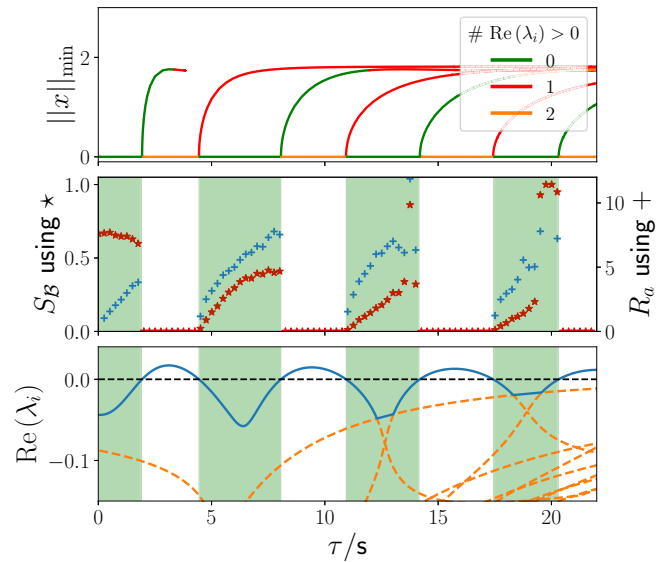


FIG. 8. Global and local stability of the delayed dynamical system (20) as a function of the delay τ . Top: Minimal 2-norm of the distance of attractors to the fixed point $\|x\|_{\min}$. The different colors indicate the number of unstable eigenvalues with green, red, and orange indicating zero, one, and two unstable roots, respectively. Middle: Size of the basin of attraction of the fixed point S_B (red stars) and the attractor radius R_a (blue pluses). The relative basin size S_B and the attractor radius R_a were computed by sampling $E = 2500$ values, which define the constant initial functions, at random from the square $[-\pi, \pi] \times [-3, 3] \text{ s}^{-1}$ for every delay τ . Bottom: The real part of the dominant eigenvalue (i.e., the λ_i with the largest real part) of the Jacobian evaluated at the fixed point is shown by the solid blue line. The orange dashed lines show the real part of additional eigenvalues $\text{Re}(\lambda_i)$. Green shaded areas in the middle and bottom panels show τ regions where the fixed point is linearly stable.

results of the linear stability analysis are given by evaluating the approximate eigenvalue spectrum using Chebyshev discretization. Furthermore, we determined the curves on which a bifurcation occurs and classified the consecutive Hopf bifurcations by evaluating the first Lyapunov coefficients with the help of DDE-BIFTOOL. The changes in stability are always accompanied by a change (i.e., an increase or decrease) in two unstable eigenvalues which is characteristic of Hopf bifurcations. The dotted black lines in Fig. 9 show the parameter value used in Figs. 6, 7, and 8, and the gray hatched area in the bottom panel of Fig. 9 gives the region in parameter space where the fixed point is not stable. Note that for larger k_p an additional critical curve exists that limits the maximal delay that the system can tolerate. This mode, in addition to the repeating critical curves that give rise to the changing super- and subcritical Hopf bifurcations, shapes the stability chart and determines regions with stable and unstable fixed points. Notably, this mode corresponds to a mechanism of instability other than the resonance effect and is discussed in Ref. [24]. The attractor radius (see the bottom panel in Fig. 9) shows a similar behavior to what we have seen previously. It increases between two regions where no stable fixed point can be found with increasing delay τ and reaches a maximum slightly before stability is lost. Additionally, there are regions in parameter space where the dynamics does not relax to any

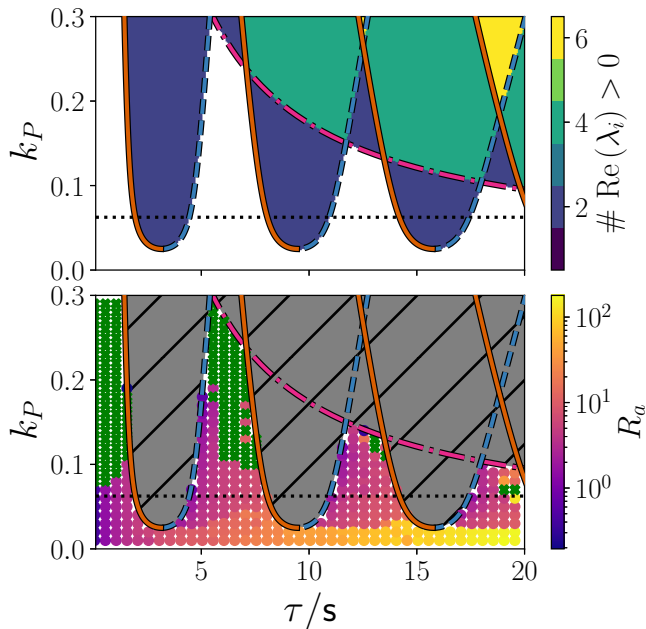


FIG. 9. Stability chart as function of k_P and τ . The number of unstable eigenvalues, i.e., eigenvalues λ_i with a real part bigger than zero, obtained from the linear stability analysis via Chebyshev discretization and the attractor radius R_a are shown in the top and bottom panels, respectively. The attractor radius R_a was computed by randomly sampling $E = 1600$ values, which define the constant initial functions, in the square $[-\pi, \pi] \times [-3, 3] \text{ s}^{-1}$ for every combination of the delay τ and the gain k_P . Parameter combinations for which all simulations with the chosen initial functions returned to the fixed point are shown as green crosses in the bottom panel. Regions in parameter space where no stable fixed point is found are indicated by the gray hatched areas. Critical curves in parameter space on which an eigenvalue has a zero real part were determined by using the software DDE-BIFTOOL. The solid orange lines and the dashed blue lines show consecutive super- and subcritical Hopf bifurcations, respectively. The dashed-dotted pink lines show the location of an additional bifurcation, which further limits the region with a stable fixed point for large k_P . The k_P value used in Figs. 6, 7, and 8 is indicated by the black dotted lines.

stable attractor other than the stable fixed point for the chosen initial functions (see green crosses in Fig. 9). This can be attributed to a bifurcation of the limit cycles, which highlights again that the stability of a fixed point depends crucially on how different attractors interact to shape the stability chart.

V. DISCUSSION AND CONCLUSION

Summarizing, we have demonstrated a case where local and global stability analyses give contrarian results: Here, large basin-of-attraction volumes coincide with vanishing linear stability at a supercritical Hopf bifurcation. Critically, we have shown that this effect not only is found in basic toy systems but also emerges in more complex anharmonic oscillators and in (delayed) power grid dynamics.

With our work, we have substantially expanded upon earlier advances, which noted the “perfect stability” in delayed power systems [15,24]. We have stressed the critical role of Hopf bifurcations and the interplay between growing

limit-cycle orbits and the basin of attraction of a stable fixed point. This correspondence is obvious for two-dimensional systems where an unstable limit cycle strictly divides the phase space. Nevertheless, we have shown that this correspondence still holds for more complex dynamical systems.

To further solve the apparent paradox of two conflicting stability statements, we might hypothesize an analogy to phase transitions, also observed in bifurcations, the “critical slowing down” [39]. When the dynamical system approaches the bifurcation, all limit cycles are far away from the stable fixed point, and the size of the basin of the fixed point is large. However, this convergence will be slower than for smaller basins (as indicated by vanishing linear stability). Hence we observe a transition from an initial steep (high linear stability) but narrow (small global stability) basin to a flat (low linear stability) and wide (high global stability) basin.

Our results are interesting both from a dynamical system perspective and from an application point of view: If system parameters are well controlled and eventual convergence is the main goal, operating a dynamical system close to the unstable bifurcation point could be desirable, as many perturbations, even large ones, will still converge eventually to the stable state. Meanwhile, if a quick convergence is desired, e.g., in power grid control, operation should be far away from the bifurcation point, while keeping in mind that large deviations in phase space are dangerous and could drive the system away from its desired state; hence tight control of the system to ensure its proximity to the fixed point is necessary at all times.

With this contribution, we have shed some light on conflicting statements from linear and basin stability. Still, many open questions remain. In the future, it would be interesting to observe whether this contrarian effect of local and global stability can also be shown for other bifurcations and basins of limit cycles (in addition to basins of fixed points). Additionally, future studies could include an extension of the power grid model by adding more details of the currently used control mechanisms and more complex topologies to see how the local stability and global stability behave. Here, larger systems with heterogeneously distributed inertia are of special interest, since future power systems need to deal with renewable generation by solar and wind power being placed at locations with the highest potential yield. Thus regions with a high share of fluctuating renewables supply a considerably low amount of inertia. Knowing how the local and global stability is affected by these developments and how to choose control parameters or delays that guarantee a stable system could play a vital role in designing a robust future power system. Future work will have to investigate in which other systems, e.g., without Hopf bifurcations, the contrarian stability assessment emerges.

ACKNOWLEDGMENTS

We thank Leonardo Rydin Gorjão for stimulating discussions and proofreading the manuscript. We gratefully acknowledge support from the German Federal Ministry of Education and Research (BMBF) via the project CoNDyNet2 (Grant No. 03EK3055B), from the Deutsche Forschungsge-

meinschaft (DFG, German Research Foundation) via Grant No. 491111487, and from the Helmholtz Association via the Networking Fund through Helmholtz AI, under Grant No. VH-NG-1727 and via the project “Uncertainty Quantification From Data to Reliable Knowledge (UQ)” with Grant No. ZT-I-0029. P.C.B. acknowledges the support of the German Federal Ministry for Economic Affairs and Energy (BMWi) via the project DYNAMOS (Grant No. 03ET4027A), in which

parts of the methodology for the stability analysis of the power grid model were developed at the DLR Institute of Networked Energy Systems. Parts of the simulations were performed at the HPC Cluster CARL, located at the University of Oldenburg (Germany) and funded by the DFG through its Major Research Instrumentation Programme (INST 184/157-1 FUGG) and the Ministry of Science and Culture (MWK) of the state of Lower Saxony.

-
- [1] S. H. Strogatz, *Nonlinear Dynamics and Chaos: With Applications to Physics, Biology, Chemistry, and Engineering* (CRC, Boca Raton, FL, 2018).
- [2] T. Gross, L. Rudolf, S. A. Levin, and U. Dieckmann, Generalized models reveal stabilizing factors in food webs, *Science* **325**, 747 (2009).
- [3] T. M. Lenton, H. Held, E. Kriegler, J. W. Hall, W. Lucht, S. Rahmstorf, and H. J. Schellnhuber, Tipping elements in the Earth’s climate system, *Proc. Natl. Acad. Sci. USA* **105**, 1786 (2008).
- [4] D. Witthaut, F. Hellmann, J. Kurths, S. Kettemann, H. Meyer-Ortmanns, and M. Timme, Collective nonlinear dynamics and self-organization in decentralized power grids, *Rev. Mod. Phys.* **94**, 015005 (2022).
- [5] P. Hartman, A lemma in the theory of structural stability of differential equations, *Proc. Am. Math. Soc.* **11**, 610 (1960).
- [6] S. Arik, An analysis of global asymptotic stability of delayed cellular neural networks, *IEEE Trans. Neural Networks* **13**, 1239 (2002).
- [7] Z. Wang, Y. Liu, and X. Liu, On global asymptotic stability of neural networks with discrete and distributed delays, *Phys. Lett. A* **345**, 299 (2005).
- [8] A. Selivanov, J. Lehnert, A. Fradkov, and E. Schöll, Adaptive time-delayed stabilization of steady states and periodic orbits, *Phys. Rev. E* **91**, 012906 (2015).
- [9] N. Barabanov, J. Schiffer, R. Ortega, and D. Efimov, Conditions for almost global attractivity of a synchronous generator connected to an infinite bus, *IEEE Trans. Autom. Control* **62**, 4905 (2017).
- [10] E. Ott, Basin of attraction, *Scholarpedia* **1**, 1701 (2006).
- [11] H. E. Nusse and J. A. Yorke, Basins of attraction, *Science* **271**, 1376 (1996).
- [12] D. A. Wiley, S. H. Strogatz, and M. Girvan, The size of the sync basin, *Chaos* **16**, 015103 (2006).
- [13] P. J. Menck, J. Heitzig, N. Marwan, and J. Kurths, How basin stability complements the linear-stability paradigm, *Nat. Phys.* **9**, 89 (2013).
- [14] A. N. Michel, L. Hou, and D. Liu, *Stability of Dynamical Systems* (Springer, New York, 2008).
- [15] B. Schäfer, C. Grabow, S. Auer, J. Kurths, D. Witthaut, and M. Timme, Taming instabilities in power grid networks by decentralized control, *Eur. Phys. J.: Spec. Top.* **225**, 569 (2016).
- [16] X. Chen and J. E. Cohen, Global stability, local stability and permanence in model food webs, *J. Theor. Biol.* **212**, 223 (2001).
- [17] L. V. Gambuzza, F. Di Patti, L. Gallo, S. Lepri, M. Romance, R. Criado, M. Frasca, V. Latora, and S. Boccaletti, Stability of synchronization in simplicial complexes, *Nat. Commun.* **12**, 1255 (2021).
- [18] F. Hellmann, P. Schultz, C. Grabow, J. Heitzig, and J. Kurths, Survivability of deterministic dynamical systems, *Sci. Rep.* **6**, 29654 (2016).
- [19] Union for the Co-ordination of Transmission of Electricity, *Policy 1: Load-Frequency Control and Performance*, UCTE Operation Handbook (UCTE, Brussels, 2004).
- [20] Union for the Co-ordination of Transmission of Electricity, *Appendix 1: Load-Frequency Control and Performance*, UCTE Operation Handbook (UCTE, Brussels, 2004).
- [21] Union for the Co-ordination of Transmission of Electricity, *Policy 1: Load-Frequency Control and Performance*, UCTE Operation Handbook (UCTE, Brussels, 2009).
- [22] J. Machowski, J. Bialek, and J. Bumby, *Power System Dynamics: Stability and Control* (Wiley, New York, 2011).
- [23] A. Ulbig, T. S. Borsche, and G. Andersson, Impact of low rotational inertia on power system stability and operation, in *Proceedings of the 19th IFAC World Congress*, IFAC Proceedings Vol. 47 (Elsevier, New York, 2014), pp. 7290–7297.
- [24] B. Schäfer, M. Matthiae, M. Timme, and D. Witthaut, Decentral smart grid control, *New J. Phys.* **17**, 015002 (2015).
- [25] P. C. Böttcher, A. Otto, S. Kettemann, and C. Agert, Time delay effects in the control of synchronous electricity grids, *Chaos* **30**, 013122 (2020).
- [26] L. Vanfretti, R. García-Valle, K. Uhlen, E. Johansson, D. Trudnowski, J. W. Pierre, J. H. Chow, O. Samuelsson, J. Østergaard, and K. E. Martin, Estimation of eastern Denmark’s electromechanical modes from ambient phasor measurement data, *Proceedings of the 2010 IEEE Power Engineering Society General Meeting* (IEEE, Piscataway, NJ, 2010), pp. 1–8.
- [27] M. Klein, G. J. Rogers, and P. Kundur, A fundamental study of inter-area oscillations in power systems, *IEEE Trans. Power Syst.* **6**, 914 (1991).
- [28] Union for the Co-ordination of Transmission of Electricity, Final Report: System Disturbance on 4 November 2006, <https://eepublicdownloads.entsoe.eu/clean-documents/pre2015/publications/ce/otherreports/Final-Report-20070130.pdf>.
- [29] A. Amann, E. Schöll, and W. Just, Some basic remarks on eigenmode expansions of time-delay dynamics, *Physica A (Amsterdam)* **373**, 191 (2007).
- [30] W. Michiels and S. Niculescu, *Stability, Control, and Computation for Time-Delay Systems: An Eigenvalue-Based Approach*, 2nd ed. (Cambridge University Press, Cambridge, 2014).
- [31] D. Breda, S. Maset, and R. Vermiglio, Pseudospectral differencing methods for characteristic roots of delay differential equations, *SIAM J. Sci. Comput.* **27**, 482 (2005).

- [32] E. Jarlebring, The spectrum of delay-differential equations: numerical methods, stability and perturbation, Ph.D. thesis, Institut Computational Mathematics, Technische Universität Braunschweig, 2008.
- [33] J. Sieber, K. Engelborghs, T. Luzyanina, G. Samaey, and D. Roose, DDE-BIFTOOL Manual - Bifurcation analysis of delay differential equations, [arXiv:1406.7144](https://arxiv.org/abs/1406.7144) [math.DS].
- [34] M. Bosschaert, B. Wage, and Y. Kuznetsov, Description of the extension ddebiftool_nmfm, https://ddebiftool.sourceforge.net/doc/nmfm_extension_description.pdf, 2015.
- [35] S. Leng, W. Lin, and J. Kurths, Basin stability in delayed dynamics, *Sci. Rep.* **6**, 21449 (2016).
- [36] T. H. Scholl, L. Gröll, and V. Hagenmeyer, Time delay in the swing equation: A variety of bifurcations, *Chaos* **29**, 123118 (2019).
- [37] T. H. Scholl, V. Hagenmeyer, and L. Gröll, On norm-based estimations for domains of attraction in nonlinear time-delay systems, *Nonlinear Dyn.* **100**, 2027 (2020).
- [38] P. Schultz, P. J. Menck, J. Heitzig, and J. Kurths, Potentials and limits to basin stability estimation, *New J. Phys.* **19**, 023005 (2017).
- [39] J. R. Tredicce, G. L. Lippi, P. Mandel, B. Charasse, A. Chevalier, and B. Picqué, Critical slowing down at a bifurcation, *Am. J. Phys.* **72**, 799 (2004).